SENSORS

Haptic perception using optoelectronic robotic flesh for embodied artificially intelligent agents

Jose A. Barreiros[1], Artemis Xu[2], Sofya Pugach[2], Narahari Iyengar[2], Graeme Troxell[1], Alexander Cornwell[2], Samantha Hong[3], Bart Selman[4], Robert F. Shepherd[2]*

Flesh encodes a variety of haptic information including deformation, temperature, vibration, and damage stimuli using a multisensory array of mechanoreceptors distributed on the surface of the human body. Currently, soft sensors are capable of detecting some haptic stimuli, but whole-body multimodal perception at scales similar to a human adult (surface area ~17,000 square centimeters) is still a challenge in artificially intelligent agents due to the lack of encoding. This encoding is needed to reduce the wiring required to send the vast amount of information transmitted to the processor. We created a robotic flesh that could be further developed for use in these agents. This engineered flesh is an optical, elastomeric matrix "innervated" with stretchable lightguides that encodes haptic stimuli into light: temperature into wavelength due to thermochromic dyes and forces into intensity due to mechanical deformation. By exploiting the optical properties of the constitutive materials and using machine learning, we infer spatiotemporal, haptic information from light that is read by an image sensor. We demonstrate the capabilities of our system in various assemblies to estimate temperature, contact location, normal and shear force, gestures, and damage from temporal snapshots of light coming from the entire haptic sensor with errors <5%.

INTRODUCTION

In living beings, the haptic system, often called touch, has been defined as the ability of the individual to sense the world adjacent to them by use of their body (*1*). Temperature, contact, pressure, damage, vibration, shear, and so on are felt simultaneously as intertwined, encoded qualities of the agent's interaction with an external object (*2*, *3*). The flesh is the organ that encodes the stimuli from the agent-object interface as a common language using an embedded, multisensory array of mechanoreceptors. Furthermore, this encoding is directly responsible for creating salience (*4*–*7*) and meaning through interactions with objects in the environment (*8*). For our purposes, salience is given by the object's distinguishing physical properties (e.g., density, stiffness, etc.), and meaning is the agent's interpretation of these qualities (e.g., warm or cold, hard or soft, and safe or threatening). Encoding of multimodal stimuli is needed to reduce the amount of data transmitted over the finite number of connections physically allowed and still retain the richness of information communicated from lower perceptual levels (i.e., mechanoreceptors) to higher ones (i.e., the brain).

This information encoding is lacking in embodied, artificially intelligent (AI) agents (i.e., robots). At present, most sensing systems are activated individually and read sequentially. Although there are multimodal, haptic, rigid sensors (*9*–*13*), we focus on soft sensors because, as they are pressed, they spread across and conform to a surface and capture more information about the object. Most of these sensors measure stimuli separately: mechanical strain for force prediction (*14*–*18*) or electrical conductivity for temperature estimation (*19*, *20*). Optical techniques, which simultaneously transmit wavelength and intensity information, provide a natural pathway to output rich, intertwined data required for the agent to understand touch (e.g., temperature, pressure, location, damage, etc.). Previous work presented systems that encode mechanical deformation in light intensity using stretchable fiber optics in an elastomeric matrix (*21*–*24*). In a similar way, Van Meerbeek *et al.* (*25*) has shown that fiber optics can be read in parallel by using an image sensor. Another type of haptic system is a class of vision-based sensors [e.g., GelSight (*26*), Digit (*27*), and others that are similar (*28*–*34*)] that consist of an elastomer gel on top of a camera that sees the deformation of the gel when in contact with an object. These systems encode haptic stimuli into an image to acquire very high–resolution measurements of shape and contact forces; however, they are still measuring only mechanical deformation and tend to be impractical for large surfaces and complex geometries.

We created a soft, optical, sensing system, called robotic flesh, that encodes haptic stimuli into light. This system allows for parallel reading of multiple points on the flesh where each point carries physically concurrent, multimodal, haptic information. We take inspiration from mammals, where the encoding is based on the simultaneous activation of a high-density distribution of mechanoreceptors, free nerve endings, and cells embedded in soft tissue [~58 units cm^{-2} in the human palm (*35*)]. In our system, a multilayered soft composite encodes haptic information in light: temperature in wavelength and pressure in intensity. Randomly or uniformly distributed nerves (i.e., stretchable optical fibers) sample light from remote locations in the flesh and send this information to a complementary metal-oxide semiconductor (CMOS) image sensor chip connected to a computer. The use of waveguides allows our system to scale to cover large surfaces (the whole body of the robot) and keep the rigid electronics [image sensor, light-emitting diodes (LEDs)] compact, thus increasing the useful sensing area. The cross section of the fiber bundles and the area of the CMOS image sensor limit the number of fibers that can be placed in the body. The optimization of the system, therefore, must be made toward sensory density in the flesh and available resources for the electronics in the agent.

To make sense of this haptic information, we use machine learning (ML), because it is an effective tool for state estimation in model-free

[1]Department of Systems Science and Engineering, Cornell University, Ithaca, NY, USA. [2]Department of Mechanical and Aerospace Engineering, Cornell University, Ithaca, NY, USA. [3]Department of Electrical Engineering, Cornell University, Ithaca, NY, USA. [4]Department of Computer Science, Cornell University, Ithaca, NY, USA.
*Corresponding author. Email: rfs247@cornell.edu

sensory systems such as ours. By using this architecture, our system can sense contact location, pressure, shear, gestures, temperature, and damage purely on the basis of interaction of light with its constituting materials. From our tests, the robotic flesh has a touch positional accuracy of 1.25 mm, a force estimation with a mean absolute error (MAE) of 0.32 N, and a temperature estimation MAE of 1.12°C in the range of 15°C < T < 60°C. In addition, it has the ability to differentiate between at least three different gestures composed of shear and normal forces and can detect direct physical damage. Furthermore, after being cut once, the flesh continues to operate with 23% decrease in force sensitivity at 10 N on average over three samples (see the "Experimental procedure for material characterization in assembly 0" section in Materials and Methods).

RESULTS

System design

Hardware

The robotic flesh is based on a multilayered architecture of elastomer materials (elastic modulus ranging from 0.5 MPa < E < 1.0 MPa) with optical properties that allow for multimodal sensing. The flesh is innervated with stretchable optical fibers that sample light and project it onto an optoelectronic sensor (CMOS, OmniVision OV2710, sensitive area = 5.86 mm by 3.28 mm, electronics board size = 35 mm by 35 mm; Fig. 1A). Its structure from top to bottom consists of a stack of elastomer layers: coating A, coating B, thermochromic (color transient at low, 31°C, and high, 45°C, temperature), transmission, and coating B embedded with optical fibers.

Light is emitted by an LED into the optically clear ($I^*I_o^{-1}$ ~ 80%; fig. S1A) transmission layer (silicone gel; Gelest Inc., Oe39, n = 1.39; fig. S1B) that disperses light throughout the body. The two coating B layers of silicone rubber (Wacker Inc., M4601, n = 1.41; fig. S1B) sandwich the transmission and thermochromic layers. Above the upper coating B, a coating layer of low transmission (coating A; black-dyed Wacker M4601, $I^*I_o^{-1}$ ~ 100%; fig. S1A) covers the structure to keep ambient light from entering the system. We included upper coating B to prevent light in the transmission and thermochromic layers from being absorbed by the black pigment in coating A. We chose the M4601 elastomer for coating B because it had been used previously as cladding material for stretchable fibers (*21*). A more appropriate material choice in the future would be minimally absorbing and have a lower index of refraction than the transmission layer. The thermochromic layers change color with temperature; we accomplished this effect by combining a silicone gel (Gelest Inc., Oe39) with commercially available pigments (blue-to-colorless 31 and red-to-colorless 45, Atlanta Chemical Engineering Inc.) that transition from colored to clear at 31° and 45°C respectively. These thermochromics are made of microencapsulated Leuco dyes that undergo a first-order phase transition in response to temperature changes (*36*–*38*). We used two layers so that we could measure a continuous range of temperatures 10°C < T < 80°C. Uniformly distributed stretchable optical fibers (d = 0.5 mm, CrystalTec, Yunze Inc., Korea) sample light from within the transmission layer through the bottom coating B onto the CMOS image sensor. These fibers have high transmittance ($I^*I_o^{-1}$ ~ 95%; see the "Transmission and refraction of each material" section in the Supplementary Materials; fig. S1A) and a higher index of refraction (n = 1.54; fig. S1B) than the coating B so light is trapped because of total internal reflection. This architecture of soft, functional elastomers allows the robotic flesh to have similar mechanical properties and distributed sensing capabilities to porcine skin over the compressive strain range 0 < γ < 0.24 (see the "Compression" section in the Supplementary Materials; fig. S1C) and minimize the need for excess rigid wiring and solid-state electronics in the system. Additional design choices are discussed in the "Design considerations" section in Materials and Methods.

Software

Designing an estimator based on first principles to predict the state of the robotic flesh from measurements of light is challenging and not scalable because of the complexity of the interactions of light with the materials including reflection, refraction, transmission, coupling, and losses. Hence, we chose to use a ML approach because it is a well-known tool for state estimation of systems with complex dynamics (*25*, *39*) such as ours. An additional benefit of customizing ML models for each specific system is that they account for variability and fabrication defects. The overall system architecture for learning (Fig. 1B) follows the classic supervised learning framework where it uses observations (input) and ground truth data (annotation label) pulled from the training dataset D_{tr} to infer a model. It includes two subsystems: training and predicting. The training subsystem consists of a feature extraction and a model selection module. The feature extractor (fig. S2) pulls meaningful information from the image coming from the image sensor by capturing a red-green-blue (RGB) image frame (1280 pixels by 720 pixels by 3 pixels),

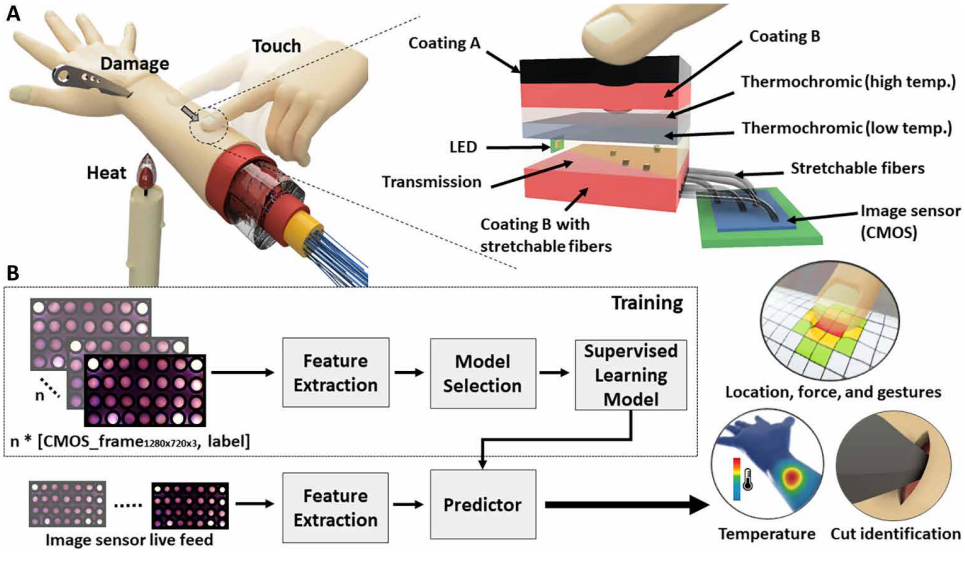

Fig. 1. Overview of the elastomeric, optoelectronic, robotic flesh. (**A**) Schematic showing the functional layers and components of the robotic flesh in an arm capable of feeling touch, damage, and heat. (**B**) ML architecture that estimates contact location, force, and temperature and identifies cut and gestures by analyzing color and intensity of light transmitted by optical stretchable fibers through the robotic flesh.

downsampling it by 50%, and filtering the frame with a previously acquired mask (fig. S3) to extract circular regions of interest corresponding to each waveguide; then, the mean RGB intensities of each region of interest are stored as features. The model selector trains various models using different supervised learning algorithms (e.g., support vector machine and random forest) and then chooses the one that performs the best on the basis of the accuracy score $\left(\frac{\text{true positive + true negative}}{\text{total}}\right)$ for classification and MAE $\left(\frac{1}{n}\sum_1^n |y_{\text{predicted}} - y_{\text{actual}}|\right)$ for regression evaluated on the validation dataset, D_{va}. Additional performance metrics were used to choose the models including precision, recall for the classifiers, and inference run time for the classifiers and regressors (see the "ML testing in assembly 2" section in Materials and Methods). Last, the predicting subsystem uses the learned model to estimate the state (e.g., contact location, temperature, force, etc.) of the system online on the basis of the chromaticity and light intensity distribution from the waveguides.

Material characterization

We characterized the optical response to primitive haptic stimuli: temperature, force, and damage using a single 3 cm–by–3 cm section of our robotic flesh with one embedded waveguide (assembly 0, Fig. 2A; see the "Fabrication of the robotic flesh" and "Experimental procedure for material characterization in assembly 0" sections in Materials and Methods). In Fig. 2B, we show that the intensity of light sampled by a waveguide increases with respect to the applied force (0 N < F < 25.2 N) at room temperature. This phenomenon likely happens because, as the sample becomes locally narrower due to the indentation, light rays bounce more often along the walls (gel-coating interface), thus increasing the chances of a ray entering a fiber. Our ray optics simulation (fig. S4; see the "Geometrical optics simulation" section in the Supplementary Materials) validates our hypothesis, showing an increase in intensity at increasing forces exerted by an indenter centered on the top of the fiber. We observed similar intensity dependence on force over all temperatures that we measured (0°C < T < 80°C; fig. S5).

For temperature characterization, we measured light from 450 < λ < 750 nm, which corresponds to the spectrum of where the CMOS image sensor is sensitive. The spectrum sampled by the waveguide shows an expected shift in wavelength corresponding to a color change of the thermochromic gels due to temperature (movie S1). In Fig. 2C, we show the normalized intensity $((\sum_R x_i + \sum_G x_i + \sum_B x_i)^{-1}\sum_{\text{range}} x_i)$, where x_i is intensity count, versus temperature (0°C < T < 90°C) in red (550 nm < λ < 750 nm), green (500 nm < λ < 650 nm), and blue (450 nm < λ < 550 nm) ranges corresponding to the RGB regions of a standard CMOS image sensor (*40*). We did this summation across five forces between 0 N < F < 25.2 N, and we see that the temperature dependency of the flesh is independent of force, allowing us to decouple the two measurements. From the graph, we infer the functional range, where the change of color is more apparent, between 15°C < T < 60°C.

In soft systems such as ours, damage such as cuts could lead to sensitivity reduction, untrustworthy measurements, or the complete loss of perception. Therefore, damage detection is important to provide causal information for the robot to, for example, reject measurements from faulty portions of the sensor, learn from the dangerous experience, or avoid further damage. As shown in Fig. 2D, a cut (width = 0.1 mm, length = 2 cm, and depth = 1 cm) made by a blade can be identified by a characteristic signature in the intensity time series. This signature consists of an up-peak followed by a particularly

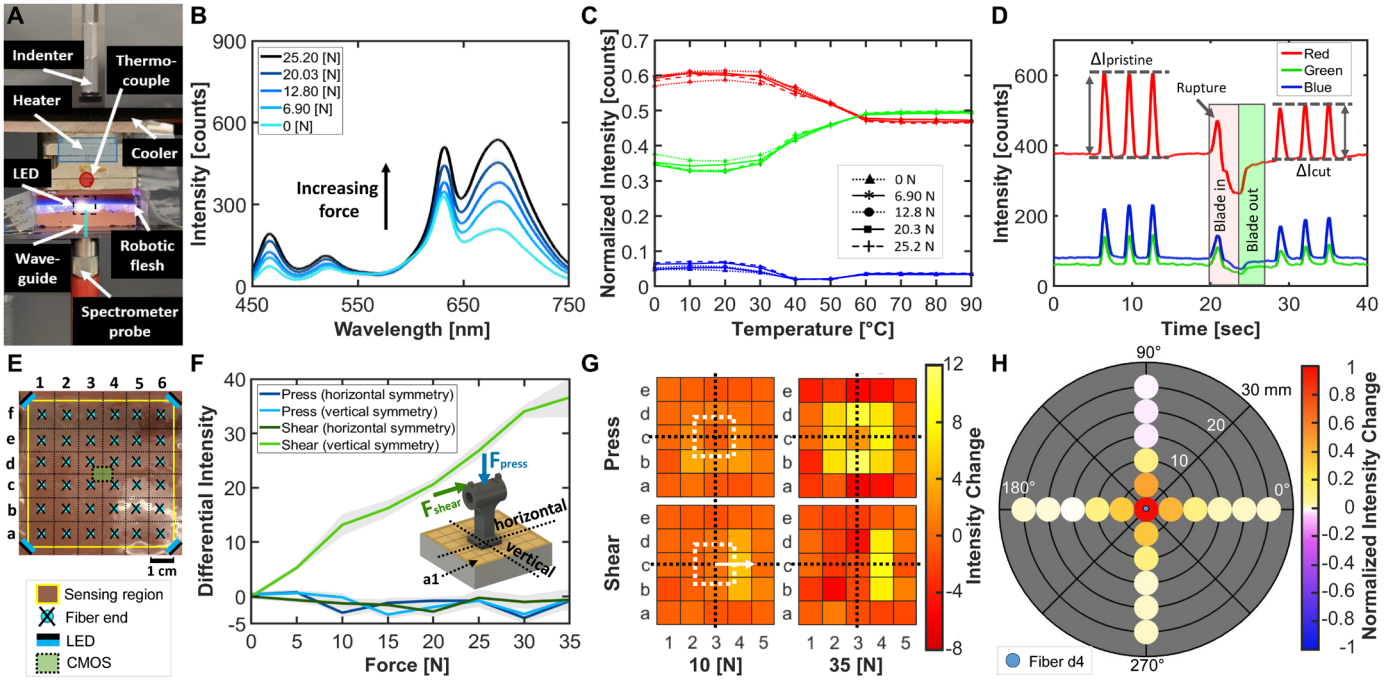

Fig. 2. Sensor characterization to various haptic stimuli. (**A**) Experimental setup used to characterize the response of a robotic flesh sample with one fiber (assembly 0) to changes in (**B**) force at room temperature (22°C) and (**C**) temperature at various indentation forces. (**D**) Response of the sample to a blade cut of 20 mm length and 10 mm depth. (**E**) Testbed (assembly 1) with 36 fibers used to characterize the response to shear and pressing. (**F**) Differential intensity at various forces for shear and pressing of an applicator centered at segment c3. (**G**) Heatmaps showing the light intensity change of the fibers for shear and pressing at 10 and 35 N with dotted symmetry lines for calculating differential intensity and a white dotted box to show the placement of the applicator. (**H**) Receptive field of a fiber for pressing at 20 N.

large down-peak (below the steady-state intensity). From observing a video of the cut (movie S2), we see that the up-peak corresponds to the point when the first layer of the flesh ruptures and the down-peak happens when the blade starts coming out of the flesh. The instantaneous decrease in intensity during cutting is explained by the interference of the sharp object (such as a knife) with the light rays inside the flesh. The permanent decrease in sensitivity after cutting is explained by the presence of cracks in the optical layers. Even after a large cut, the flesh can sense touch, albeit with decreased force sensitivity. The intensity of light $\left(I = \frac{\text{red + green + blue}}{3}\right)$ sensed after the cut decreased by $1 - \frac{\Delta\text{cut}}{\Delta\text{pristine}} = 1 - \frac{I_{\max_{\text{after cut}}} - I_{\text{baselineafter cut}}}{I_{\max_{\text{before cut}}} - I_{\text{baselinebefore cut}}} = 0.23$ for the same indentation force (10 N).

Because a monolithic volume of elastomer allows for continuum displacement of its surface and propagation of this stress and strain to its subsurface, we chose to use this robotic flesh to measure both normal and shear force input. We evaluated pressing and shearing using a 7 cm–by–7 cm testbed of our robotic flesh with 36 waveguides uniformly distributed (assembly 1, Fig. 2E; 0.73 fibers cm^{-2}; see the "Fabrication of the robotic flesh" and "Experimental procedure for material characterization in assembly 1" sections in Materials and Methods). This array is important because we observe shear primarily by changes in light intensity patterns across the flesh surrounding the applicator. In Fig. 2F, we show the differential intensity of light sampled by the fibers across varying symmetry lines (i.e., horizontal and vertical) aligned at the center of the applicator for pressing and shear forces at room temperature (fig. S6A shows the experimental setup; see the "Experimental procedure for material characterization in assembly 1" section in Materials and Methods). The differential intensity is defined as the difference in the sums of the signals on each side of the symmetry line minus the ones on the other side (for horizontal symmetry: $\text{abs}(\sum_{i_{\text{top}}} I_{i_{\text{top}}} - \sum_{j_{\text{bottom}}} I_{j_{\text{bottom}}})$ and for vertical symmetry: $\text{abs}(\sum_{i_{\text{right}}} I_{i_{\text{right}}} - \sum_{j_{\text{left}}} I_{j_{\text{left}}})$). Figure 2G shows the heatmaps of the light intensity changes ($I - I_{\text{steady state}}$; steady state: $F_{\text{shear}} = 0$ N, $F_{\text{press}} = 0$ N, $I \in [0,255]$) from the fibers surrounding the applicator at 10 and 35 N (see fig. S6, B and C, for other forces). As seen in Fig. 2F, only shear produces an increasing differential intensity in the shear direction (vertical symmetry) with increasing force. We suspect that this effect occurs as depicted in a simplified system with two fibers shown in fig. S6D. As we shear (in this case, to the right), the indenter gets farther from the fiber opposite to the shear direction (fiber A), and it gets closer to the fiber in the shear direction (fiber B). The rays, therefore, are more likely to enter the receptive field of fiber B than fiber A as we have seen in the simulation (fig. S4). From the heatmap of the pressing, we see that the intensities of the fibers directly below or close to the applicator (b2-d4) show an increase in intensity with increasing force in accordance with Fig. 2B; the fibers far from the applicator see a decrease in intensity, suggesting that shadows are cast on these fibers. Unexpectedly, the fibers closer to the edge of the applicator see a higher change of intensity than the fiber directly below. This happens potentially because of the presence of corners that could direct more rays into the lightguide because of the larger variety of angles compared to a flat surface.

To characterize the receptive field of a single fiber, we calculated the normalized intensity change $\left(\kappa\kappa = \frac{\Delta I}{\Delta I_{\max}}; \Delta I = I - I_{\text{steady state}}\right.$ and $\Delta I_{\max} = I_o - I_{\text{steady state}}$; I_o: intensity when pressing directly above the fiber$\left.\right)$ of the light sampled by a specific fiber when pressed with $F = 20$ N (Fig. 2H; see fig. S7A for other forces). We performed this procedure at locations from $\delta\delta$=0 to 25 mm, where $\delta\delta$ is the distance from the center of the fiber end to the center of the circular indenter ($d = 5$ mm), at angles 0°, 90°, 180°, and 270° (see the "Experimental procedure for material characterization in assembly 1" section in Materials and Methods). We show that $|\kappa\kappa|$ decreases as we move radially away from the center of the fiber. We define ζ as the maximum distance at which a press can be read from a fiber ($\zeta = \delta\delta$, when $|\kappa\kappa| < 0.1$). For assembly 1, the minimum readable signal is at $\zeta = 10$ mm where $|\kappa\kappa| = 0.074$ (averaged over all forces measured in all angle directions; fig. S7B). Therefore, to ensure that there are no immeasurable zones, fibers should be located within $2\zeta = 20$ mm apart from each other in any direction. This distance could change depending on the system characteristics such as the intensity of the LEDs, sensitivity of the CMOS image sensor, diameter of the fiber, thickness of the optical layers, and geometry.

Robotic flesh haptic characterization

We characterized the sensing capabilities of our flesh using an 11 cm–by–7.5 cm testbed that includes 28 uniformly distributed waveguides (assembly 2; fig. S8; 0.34 fibers cm^{-2}; see the "Fabrication of the robotic flesh" section in Materials and Methods) by measuring the positional accuracy of single- and multitouch pressing, spatial resolution for single pressing, classification accuracy for gesture identification, accuracy of cut detection, and error for force and temperature estimation.

The estimation of contact location was framed as a ML classification problem where a model trained on labeled data ($\{X, Y\}$, $x \in X$, $x = [a_1, .., a_n]$, a_i : mean intensity of fiber i and $y \in Y$: ID of indented segment s) assigns a unique label $y \in Y$ to the input data x. Figure 3 (A to C) shows the confusion matrix of the predicted versus the ground truth labels for the testing dataset D_{te} where the color corresponds to the classification accuracy. For single-touch location on a 77-square grid using a circular indenter ($d = 1$ cm), the classification accuracy is 1.00 (Fig. 3A). For multitouch location on a nine-square grid using the same indenter, the classification accuracies are 1.00, 1.00, and 0.98 for single, double, and triple touch, respectively (Fig. 3B). We evaluated the resolution $\Gamma_{\min}$ of single-touch location in 16 segment grids (16, 4, 2, and 1 cm^2) with corresponding indenters of $d = 10$, 5, 2.5, and 1.25 mm; smaller indenters were not used because they would puncture the flesh. The classification accuracies are 1.00, 1.00, 1.00, and 0.99 from largest to smallest indenter, respectively (Fig. 3C). These data show that we can identify the position of pressing on a grid with at least 1.25-mm cell spacing. In an indirect comparison, the human hand can identify two simultaneous pressings as individual contacts when 2.2 mm apart at the index fingertip (*41*).

For gesture estimation, we used a classifier that takes a set of features of the monochrome mean intensity time series using a 500-ms sliding window (*42*) (see the "ML testing in assembly 2" section in Materials and Methods). The model identifies the absence of touch (steady state, SS) and three distinct gestures that were performed manually on the flesh: pinching, sliding, and twisting that include normal and shear forces. Figure 3D shows the confusion matrix with an accuracy of 1.00 for all the classes.

Force and temperature estimation were framed as a regression problem where the model estimates a continuous value ($w \in \mathbb{R}$) based on the input x. In Fig. 3E, we show the absolute error of the force estimation for a single touch between $0 < F < 16$ N using an indenter ($d = 1$ cm). The MAE is 0.32 N across the entire range, defining the force resolution of our system. In comparison, humans are able to distinguish two subsequent forces at a difference of 0.18 N at the fingertip (*43*).

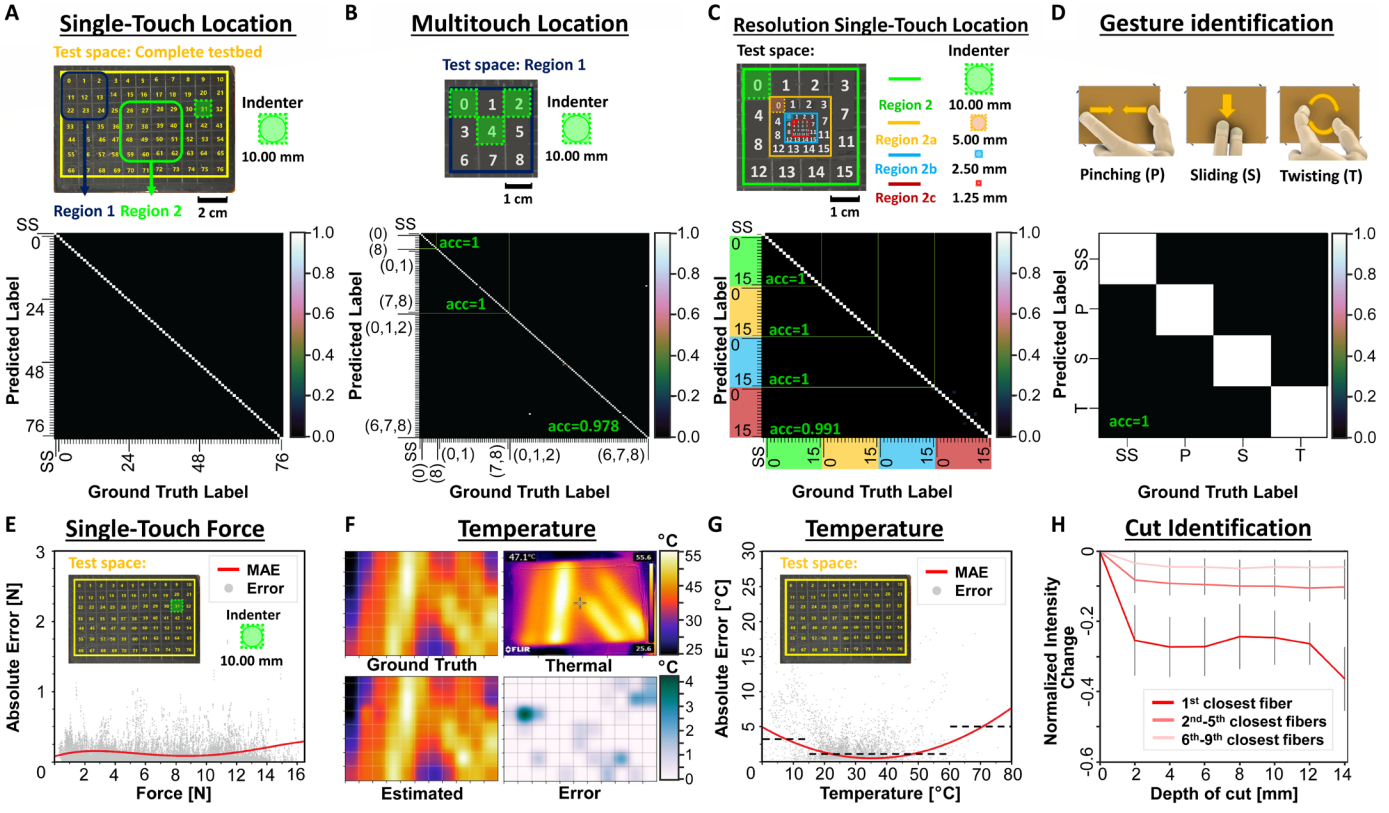

Fig. 3. Results of the estimations of haptic stimuli on a rectangular testbed. Schematic showing the test spaces and the normalized confusion matrices for the estimation of (**A**) single-touch location; (**B**) multitouch location for single, double, and triple touch; (**C**) single-touch location at different indenter diameters to evaluate resolution; and (**D**) gesture identification. (**E**) MAE distribution for force estimation. (**F**) Example of temperature estimation. (**G**) MAE distribution for temperature estimation. Dashed lines show the averaged MAE in the given range. (**H**) Normalized intensity change of the closest fibers to a cut versus depth of cut exerted with a blade (width = 1.1 cm). SD ($n = 10$ cuts) is shown in gray.

For temperature, we use 77 regressors in parallel to estimate the local temperature of each segment (a = 1.00 cm^2) of the flesh. The ground truth temperature was acquired by using a thermal camera (FLIR Inc., TG165). Figure 3F shows the ground truth, estimation, and error heatmaps along with the thermal image of the robotic flesh after touching a flexible heater (see the "ML testing in assembly 2" section in Materials and Methods; fig. S9). We quantify these results in Fig. 3G where we show the distribution of the absolute error versus quasi-static surface temperature ($0 < T < 80$°C) for each segment. From these data, we validate that our system performs better in the range $15 < T < 60$°C with an average error of 1.12°C, consistent with the measurement of color change versus temperature in Fig. 2C. The other ranges $0 < T < 15$°C and $60 < T < 80$°C experience an averaged MAE of 3.90° and 5.41°C, respectively. Lower errors could be achieved by using a combination of thermochromic dyes with transition temperatures uniformly distributed along the desired range.

We exerted cuts on the flesh at various depths using a blade to cause damage to the robotic flesh (width = 11 mm and thickness = 0.1 mm; fig. S10A; see the "Damage characterization in assembly 2" section in Materials and Methods). In Fig. 3H, we show the average over 10 cuts (fig. S10B) of the normalized intensity change $\left(\frac{1}{n}\sum_{1}^{n}\frac{I_i - I_{i_{\text{pristine}}}}{I_{i_{\text{pristine}}}}; I = \frac{R+G+B}{3}; I_i : \text{intensity of the } i\text{th closest fiber}\right)$ for the first closest fiber, the second to fifth closest fibers, and the sixth to ninth closest fibers to the center of the cut (fig. S10C). A cut produces an intensity drop in the closest fibers to it; a larger drop is evidenced at the first closest fiber and the intensity decreases as the radial distance to the fiber increases. We can also infer that the minimum cut that can be identified is at 2-mm depth. We point out that a very shallow cut and a very hard pressing can create similar levels of intensity drop although in different fibers; however, we believe that a more sophisticated algorithm that detects features in the time series (as in the gestures estimator) could pick up the characteristic signature of cut.

Demonstration of haptic sensing in a human-scale forearm

We designed a forearm (assembly 3; fig. S11) to showcase the scalability of the system to larger embodiments and its flexibility to be shaped in more complex geometries. The forearm consists of a three-dimensionally (3D) printed, rigid lattice that serves as the structural support (bone) for the robotic flesh and a conduit for the optical waveguides. We were able to thread 120 waveguides (0.53 fibers cm^{-2} of bone surface) limited by the sensing area of the CMOS image sensor; although the fibers were manually placed to make it somewhat uniformly distributed, the mapping from the fiber location in the coating B layer to the image sensor is random. We cast the elastomeric layers of the robotic flesh following the same procedure as that for assemblies 1 and 2 (see the "Fabrication of the robotic flesh" section in Materials and Methods). For sensing evaluation, we divided the surface of the forearm into 59 segments and used two acrylic rings to hold it in place (Fig. 4A).

To demonstrate simultaneous online estimation of touch location and force, we randomly selected eight segments and captured training data. We acquired the training dataset by manually indenting the segments using a metal rod (d = 5 mm) with forces ranging from 0 < F < 20 N in steps of 1.0 N, 20 times. The indenter was connected to a load cell (Sparkfun Electronics Inc.; 5-kg TAL220B load cell) for ground truth recordings. We then trained a model for touch location and another for force and used them in parallel for estimation. For testing, we pressed four segments in a random sequence and recorded a video showing the poking location (movie S7) and force estimation in a graphic reconstruction of the forearm (Fig. 4A and movie S8). We also show the time series for ground truth and force estimation for one segment (Fig. 4B and movie S8). We evaluated the location and force estimations on the testing dataset, obtaining 97% positional accuracy and MAE = 0.24 N, respectively. We recorded a video of our script working in real time, showing the waveguide signals and the cut identification for the forearm when damaged with a scalpel (Fig. 4C and movie S10). Damage was detected by simply looking at drops in the intensity signal greater than 10% in at least four fibers or a large drop, more than 40%, in at least one fiber. This pattern is consistent with the results from the cut experiment in Fig. 3H. For temperature, we selected a region of the forearm (Fig. 4D and movie S9) and divided it into a 6-by-5 grid. We then acquired a training dataset (n = 624) for temperatures from 20 < T < 75°C by using a flexible heater and Peltier plate. For testing, we heated the region with a heat gun for about 60 s, and, while the flesh cooled down, we captured a sequence of thermal images and saved the frames for 101.7 s at a sampling rate of 15 frames min^{-1} (movie S9). We show a comparison of ground truth to estimated temperature and the error for frames sampled every ~19 s (Fig. 4D). From these data, we successfully predict the temperature with a MAE of 2.39°C.

DISCUSSION

We developed a robotic flesh that can encode rich, multisensory, and haptic stimuli into the color and intensity of propagating light rays by exploiting the optical properties of the constitutive materials. We sampled light from within the flesh using stretchable optical waveguides that serve as nerves to transport information to a CMOS image sensor to be processed at a higher perceptual level (i.e., brain). Light is interpreted by a supervised learning model to estimate temperature, location, pressure of touch, gestures, and even damage perceived in parallel from proximal and distal regions of the body. Our robotic flesh is able to identify a single-touch location with spatial resolution Γ_{min} = 1.25 mm (Γ, length of a square segment) at 5 N, at least three simultaneous pressings with 97.8% accuracy, force estimation with an error of ±0.32 N over a range of 0 < F < 16 N, cut detection with a minimum depth of 2 mm, three distinct gestures that include normal and shear forces (i.e., pinching, sliding, and twisting), and temperature with an error of ±1.12°C in the range of 15°C < T < 60°C.

The characteristics of our system are a step forward in artificial haptic perception, albeit we are currently far from the abilities of human flesh, including the ability to sense high-frequency vibration [5 to 150 Hz, Meissner corpuscles; 20 to 1000 Hz, Pacinian corpuscles (*44*)], identify static and dynamic contact, and detect rapid changes in temperature (*45*, *46*). Despite this large gap, there are many ways to improve our system. Spatial resolution for touch location, temperature, and damage estimation could be increased by embedding a greater number of waveguides and optimal allocation of them at the cost of a larger or multiple image sensors and fabrication complexity. Suggested by the high accuracy for three simultaneous touches, we believe that we could estimate multitouch location for more points if the training dataset is extended to those cases. Temperature sensing can be enhanced by optimizing the number of thermochromic layers and their geometry for the desired range and resolution. Furthermore, higher thermal conductivity of the coatings (A and upper B)

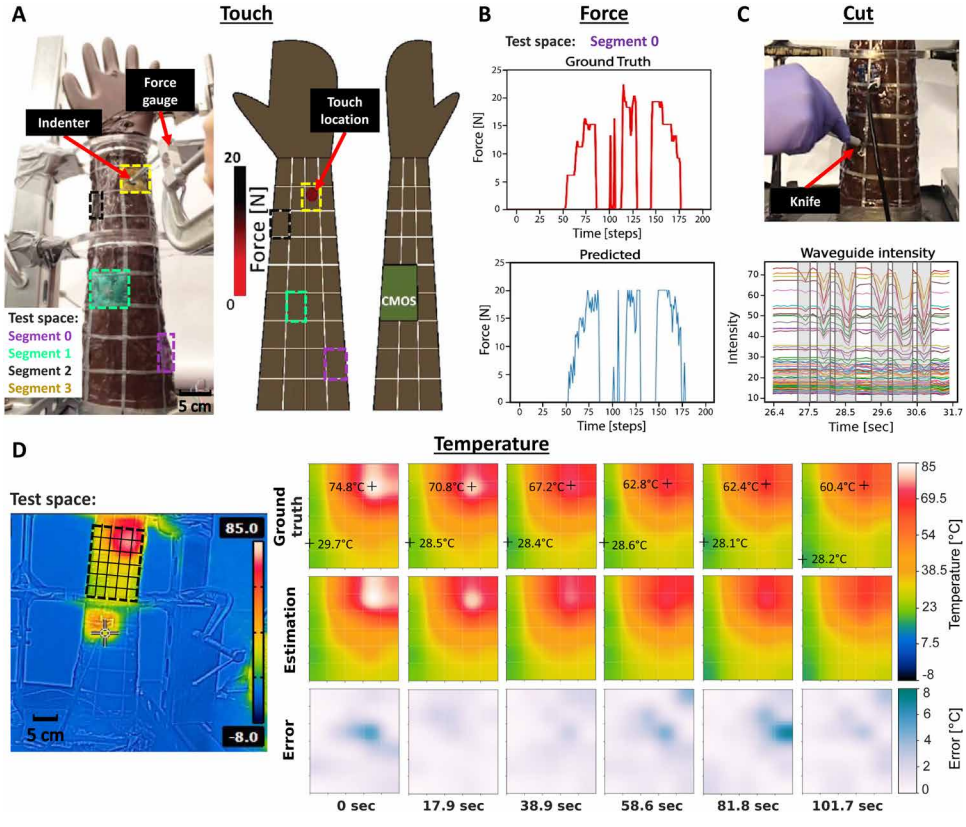

Fig. 4. Demonstration of the proposed robotic flesh in a human-scale forearm. Images showing the test space and a screenshot of the visualization for various tests. (**A**) Location and force estimation of touch. (**B**) Estimated force and ground truth reading from a force gauge of an indenter pressing on segment 0. (**C**) Identification of cuts made with a scalpel. Gray boxes show the start and end of a cut. (**D**) Temperature ground truth, estimation, and error of a sequence (101.7 s) corresponding to the cooling down of the forearm after being heated with a heat gun. The heatmap shows the visualization of a 6-by-5 matrix of temperatures with linear interpolation.

and thermochromic layers would result in faster thermal equilibrium of the system (*47*–*50*), thus allowing rapid temperature changes to be detected. Damage could be accumulated without losing sensitivity by using self-healing elastomers, but this is still an active area of research (*51*–*53*). The ability of the system to detect high-frequency force changes is limited by the sampling rate of the CMOS image sensor and computer processing speed. A specialized image sensor that is faster [e.g., On Semiconductor, LUPA3000 series, 485 (3 megapixels) to 2653 fps (307 kilopixels)] and a faster processor may permit sensing of vibration. A more sensitive image sensor could allow for longer waveguides, or less powerful LEDs. In addition, an extra sensor channel (e.g., microphone array and photodiodes) could be embedded in the structure of the system to detect quickly changing stimuli. Currently, we use the mean intensity of the region corresponding to each waveguide as features for the learning models. A higher number of sampled points in the frame could increase the sensitivity and resolution of the sensor and allow for other sensing modes (e.g., slip).

A major limitation of our work is the need for large datasets for training that is time consuming and might not be scalable in certain cases. We believe that by using our robotic flesh in an embodied AI agent, more sophisticated training algorithms can be used to reduce the amount of data provided by the designer. For example, curriculum learning (*54*), where basic skills are learned first and others are built upon them, could reduce the size of the training dataset required (e.g., learning the spatial component of temperature could be simplified by first learning to estimate touch location). Another example would be to use reinforcement learning in combination with our robotic flesh, which could form the basis of an embodied agent that can learn by itself to feel touch without supervision by touching its own body in the real world or in simulation (*55*).

In the future, the use of a whole-body robotic flesh for an embodied AI agent could allow it to recognize the boundaries of its own body by exploiting the confluent multimodal haptic data. In addition, the ability to perceive damage could lead to self-preservation behaviors that are crucial to endure long-term and autonomous missions.

MATERIALS AND METHODS

Design considerations

Layer thickness

Every layer should be as thin as possible other than the following considerations. The transmission and thermochromic layers combined need to match the LED size. The thermochromic layer should be thick enough so the color change is notable. The coating A should be thick enough so it blocks environmental light. Bottom coating B should be thick enough so sharp bends in the fibers are avoided thus reducing losses. Optimization of the layer thicknesses opens the possibility for other fabrication methods such as stencil printing. This method could allow for reduced curing time and a more compact integration of the waveguides because they can be directly printed in the robotic flesh. By doing so, the resulting device could be wrapped around the body of a robot.

Edges

Edges are necessary to input light from the LEDs into the flesh; however, no edge should remain open to the environment because ambient light could disturb the measurements. For example, in assembly 0, edges are covered with the LED flexible printed circuit board; in assemblies 1 and 2, edges are covered by the side faces of the mold; and in assembly 3, edges are covered by a top and bottom plate (fixtures A and B in fig. S11). A potential improvement to the system is to clad the edges ($n_{edge} < n_{transmission\ layer}$). Such cladding will allow the light rays to bounce back into the system, thus increasing the intensity of light within the flesh.

Fabrication of the robotic flesh

We manufactured the robotic flesh by casting thermoset elastomers into 3D-printed molds. For material characterization, we designed a 3 cm–by–3 cm sample (assembly 0; Fig. 2A) and a 7 cm–by–7 cm testbed (assembly 1; Fig. 2E). For haptic characterization, we designed an 11 cm–by–7.5 cm testbed (assembly 2; fig. S8). Last, we demonstrated the results in a human-scale forearm (assembly 3; fig. S11).

Figure S8 shows the manufacturing process of assembly 2, which is representative of the method used for assemblies 0, 1, and 3. Two support molds and a rectangular housing (fig. S8A) were 3D printed using the Carbon UMA 90 resin. The bottom mold includes holes to align stretchable waveguides (d = 0.5 mm; CrystalTec, Yunze Inc., Korea) to the sensing area of the CMOS image sensor. The top mold serves as a fixture to keep the waveguides in place while casting the silicone rubber. The housing includes four holes at the corners where high-intensity white LEDs (SZLEDCOLOR SK6812 5050 0.2 W for assemblies 1 and 2 and Betlux BL-HP20A 3 W for assembly 3) were press-fitted (fig. S8A). We first threaded 28 stretchable waveguides through the holes of the bottom mold, the housing, and the top mold. We then cast and degassed a 7-mm-thick layer of silicone rubber (Wacker M4601; coating B) in a vacuum chamber at 101 kPa (14.64 psi) for 10 min (fig. S8B). We then place it in a convection oven for 4 hours at 80°C. After curing the first layer, we removed the top and bottom support molds and trimmed both ends of the waveguides leaving the image-sensor side flush and the transmission side ~2 mm above the surface. We then cast a 6-mm-thick layer of silicone gel (Gelest Inc.; OE39 for assemblies 0, 2, and 3; see the "Note on fabrication of assembly 1" subsection), degassed, and heat cured it with the aforementioned settings. Similarly, we cast, degassed, and cured layers of blue and red thermochromic elastomer, silicone rubber (coating B), and black-dyed silicone rubber (coating A) of layer thicknesses 1.5, 1.5, 0.5, and 0.5 mm, respectively. The thermochromic silicone gels were prepared by mixing silicone gel (Gelest, Inc.; Oe39 for assemblies 0, 2, and 3; see the "Note on fabrication of assembly 1" subsection) with 0.5 weight % (wt %) red (Atlanta Chemical Engineering Inc.; red-colorless-45C), and 0.5 wt % blue (Atlanta Chemical Engineering Inc.; blue-colorless-31C) thermochromic pigments using a centrifugal mixer (Thinky ARE-310) at 2000 rpm for 60 s. Coating A was prepared by mixing 1 wt % concentration of black dye (Smooth-On Inc.; Silc Pig Black) in M4601 silicone using a centrifugal mixer at 2000 rpm for 60 s. Figure S8C shows the thicknesses of each layer of the flesh.

Last, we assembled the testbed by securing a CMOS image sensor (ELP USBFHD01 module with OmniVision OV2710) above a fan (for cooling the CMOS) and then layered the robotic flesh atop the optoelectronic assembly (fig. S8D). Environmental temperature changes could cause the CMOS to drift in intensity; thus, thermal isolation of the sensing element or in-chip temperature compensation is desired to ensure decoupling between temperature and force measurements.

Molding, when done manually, could be time consuming. However, it is a well-established industrial process suitable to fabricate consumer products at scale and has been optimized for production

time, defects, and variability (*56*, *57*). For reference, table S1 shows the approximate time that was used to fabricate assembly 2.

Note on fabrication of assembly 1

Because of material unavailability at the time, we manufactured assembly 1, Gelest Inc.; Oe39 (n = 1.39, Shore hardness 5A) was replaced with SmoothOn Inc. Solaris (n = 1.41, Shore hardness 15A) in the transmission and thermochromic layers. Solaris has a higher hardness, resulting in a stiffer overall flesh. It also has a higher index of refraction but, on the basis of how the system work, we did not expect nor see any difference in the encoding.

Experimental procedure for material characterization in assembly 0

We prepared a 3 cm–by–3 cm–by–1 cm robotic flesh sample with one waveguide in its center. We illuminated the sample by a white-light LED (SK6812 5050, 0.2 W) placed in contact with its back surface (fig. S1E). Then, we aligned the end of the waveguide to the probe of a spectrometer (Ocean Optics USB 2000+) to measure the spectrum of light.

In addition, we created a test setup that can heat, cool, and indent the surface of the sample while recording temperature and force. The test setup includes an aluminum fixture (fig. S1E) that encloses, from top to bottom, a Peltier plate for cooling (Adafruit Inc., Thermoelectric cooler ID: 1335, 12 V), a resistive flexible heater (Adafruit Inc., Electric heating pad, ID: 4308, 3.2 W), and thermocouple (Adafruit Inc., Type-K, ID: 270). The heater and cooler were connected to individual power supplies that control its temperature, and the thermocouple was connected to a logger (MYPIN TA6-SNR PID) for data visualization. To apply forces to the sample, we used a linear actuator (Actuonix Inc., P16-S, 12 V) with an indenter (circular cross section = 1 cm) attached to a force gauge (Adafruit Inc.; load cell, 10 kg; ID: 270).

Force

We first heated or cooled the sample until it reached a stable temperature in a range of 0°C < T < 80°C. We then indented it up to a force, F = 25.2 N, in five steps.

Temperature

We heated or cooled the sample to temperatures ranging from 0° < T < 90°C, while a force was applied in the range of 0 N < F < 25.2 N.

Damage

We recorded the time series of light intensity at the red, green, and blue peaks of the spectrum (630, 519, and 466 nm, respectively) for a sequence of (i) three indentations at F = 10 N, (ii) a knife cut (width = 0.1 mm, length = 20 mm, and depth = 10 mm), and (iii) three indentations at 10 N (movie S2). We repeated this experiment across three different samples and manually annotated the time series based on the video recordings with labels corresponding to the phases of cut: (i) blade in and (ii) blade out.

Experimental procedure for material characterization in assembly 1

We prepared a 7 cm–by–7 cm robotic flesh testbed with 36 waveguides uniformly distributed. We divided the surface in six-by-six segments with centers corresponding to the location of the fiber ends (Fig. 2E). The other ends of the fibers were guided to rest on top of a CMOS image sensor located at the center of the assembly.

Pressing and shear

We fabricated an applicator of 2 cm by 2 cm with a 0.3-mm-thick rubber surface (same material as coating A) to ensure high-friction contact and no slippage with the flesh surface (fig. S6A). For the pressing experiment, we attached the applicator to a digital force gauge (Nextech Inc., DFS 1000) in the normal force direction and centered it at segment c3. We then pressed on the flesh at forces from 0 < F < 35 N in steps of 5 N and recorded the average of the monochromatic pixel intensities corresponding to the circular regions of each fiber (similar to fig. S2). Each measurement was repeated 10 times with ~2-s interval time between two separate trials (intertrial time).

For the shear experiment, we mounted the applicator on an aluminum rod (r = 5 mm) as shown in fig. S6A and applied grease at the interface to reduce friction. We centered the applicator at the center of segment c3 and connected it to the aforementioned force gauge along the shear direction. We then indented the applicator into the flesh at 1 mm and sheared the flesh at forces from 0 < F < 35 N in steps of 5 N. Under these conditions, no slippage was observed. We recorded the intensities with the same procedure as for pressing. Each measurement was repeated 10 times with ~2-s intertrial time.

Figure S6 (B and C) shows the averaged heatmaps over the 10 measurements for the change of light intensity of the fibers at various pressing and shear forces. The applicator profile is shown in white dotted lines, and the shear direction is shown with a white arrow.

Receptive field

We attached a circular indenter (d = 5 mm) to a digital force gauge (Nextech Inc., DFS 1000) and centered it at segment d4. We then pressed the flesh with forces from 0 < F < 20 N at distances in the radial axis from 0 to 25 mm from the fiber end in steps of 5 mm and at polar angles from 0 to 270° in steps of 90°. We recorded the intensity of light sampled by the fiber with the same procedure as for pressing and shear. Each measurement was repeated 10 times with ~2-s intertrial time.

Figure S7A shows a polar scatter plot of the averaged normalize intensity changes over the 10 measurements at 5-, 10-, or 20-N force. In the plot, positive values show an increase in light intensity and negative values show a decrease in intensity from the intensity value at a poke centered directly on top of the fiber (shown as a blue circle). Figure S7B shows the absolute normalized intensity change averaged over 0°, 90°, 180°, and 270° angles versus radial distance measured from the center of the fiber. The SD over the 10 measurements is shown in gray.

ML testing in assembly 2

The model types, training algorithms, dataset sizes, and hyperparameters are summarized in table S3. The datasets were acquired during 15 nonconsecutive days, and the models were trained using a graphics processing unit virtual machine from Google Colab Pro (*58*). We used the classifier and regressor algorithm implementations of sklearn_API (*59*) and its grid exploration algorithm for hyperparameter optimization.

Evaluation metrics

The models were evaluated using, if applicable, accuracy, precision $\left(\frac{\text{true positive}}{\text{true positive + false positive}}\right)$, recall $\left(\frac{\text{true positive}}{\text{true positive + false negative}}\right)$, MAE, root mean square error $\left(\text{RMSE} = \sqrt{\frac{1}{n}\sum_{1}^{n}(y_{\text{predicted}} - y_{\text{actual}})^2}\right)$, and the elapsed time to run inference on a single data point $\left(\frac{1}{n}\sum_{1}^{n} t_i, t_i : \text{inference run time of the } i\text{th randomly selected point}, n = 100\right)$. Table S4 shows the summary of the performance metrics for the trained models evaluated on the testing dataset.

Single-touch location and force

We divided the testbed (assembly 2) in 77 square segments of 1 cm^2 (Fig. 3A). We then acquired three unique datasets: training (D_{tr}), validation (D_{va}), and testing (D_{te}) by poking a circular metal indenter (d = 1 cm) at forces ranging from $0 < F < 16$ N in steps of 0.25 N using a similar experiment setup as in material characterization in assembly 0 (movie S5). The process of acquiring a data point was to manually align the indenter at the center of the segment, press down, record the resultant force and the segment ID, capture the image frame, save all the values in a single data structure (i.e., segment ID, F, frame number), then release the actuator, pause for 4 s, and repeat. For each force, we pressed each segment 10 times.

Multitouch location

We selected a 3 cm–by–3 cm region of the testbed (region 1, assembly 2; Fig. 3A) and acquired D_{tr}, D_{va}, and D_{te} for steady-state (no poking) and simultaneous poking with one, two, and three circular indenters from $0 < F < 16$ N in steps of 0.5 N (Fig. 3B). This process generated 9, 36, and 84 different labels for all possible combinations for single, double, and triple touch, respectively. The process of acquiring a data point was similar to that shown above. For each force, we pressed each combination of segments 10 times.

Resolution for single-touch location

We selected four overlapping regions of 4 cm by 4 cm (region 2, assembly 2; Fig. 3A), 2 cm by 2 cm (region 2a), 1 cm by 1 cm (region 2b), and 0.5 cm by 0.5 cm (region 2c) and divided each of them into 16 segments (Fig. 3C). We then poked each segment of regions 2, 2a, 2b, and 2c with circular indenters of section d = 10, 5, 2.5, and 1.25 mm, respectively, at F = 5 N following a similar process as shown above. Smaller indenters (d < 1.25 mm) were not used because they puncture the first layer of the flesh at the force used in this experiment. For each force, we press each segment in each region 30 times.

Temperature

We divided assembly 2 into 77 square segments of 1 cm^2 and measured their temperature at the center using a thermal camera (FLIR Inc., TG165) for ground truth. Using FLIR Tools software, the temperature at the center of each segment of the flesh is extracted. This results in a 7-by-11 matrix of temperatures. In fig. S9, ground truth shows the visualization of this matrix with linear interpolation. For cooling and heating the surface of the robotic flesh, we used a resistive heater and a Peltier plate. The process of acquiring a data point was as follows: (i) Set the heater or cooler to any temperature in the range $0 < T < 80$°C, (ii) place the thermal element on top, (iii) heat or cool for 2 min, (iv) remove it, (v) let the flesh rest for 1 s, (vi) capture a thermal image and an image frame, (vii) save all the values in a single data structure (i.e., thermal image and frame), pause for ~30 s of intertrial time, and then repeat. We performed 636 heat/cool actions.

Gestures

We manually performed various gestures on the surface of the skin with our fingers. To reduce friction between the rubber surface and our fingers, we applied silicone oil (Sigma-Aldrich Inc., SKU: 317667; viscosity, 5 cSt). To increase data diversity, three participants applied the gestures at various pressures and locations but in the same orientation (as in Fig. 3D) over multiple sessions. For a single data entry, we performed a gesture for ~2.5 s while simultaneously recording the sequence of frames coming from the image sensor running at a rate of 60 fps. However, in our implementation of online inference using the learned model, the actual processing rate is 2.07 fps on average, explained as follows: (i) read an image frame, 20 ms; (ii) extract the mean intensity values, 110 ms; (iii) extract the time series features, 350 ms; and (iv) run the inference, 1.5 ms. This pipeline, coded in Python, was run on a laptop (Dell Inc., Intel Core i7-8650U CPU @ 1.90 GHz, 8GB RAM). Higher frame processing rate is desirable for robust gesture detection and can be achieved by the use of a faster computer and optimized code for the feature extraction and inference module. We captured 100 gestures for each class and waited for ~4 s between trials.

Damage characterization in assembly 2

To systematically cut the flesh, we used a z-axis stage and a stainless steel blade of width = 11 mm and thickness = 0.1 mm (fig. S10A). We performed 10 cuts (fig. S10B) at depths from 0 to 14 mm by (i) locating the blade on top of the desired cut area, (ii) lowering the z stage to the desired cut depth, (iii) recording 10 frames from the image sensor over 1 s, (iv) raising the z stage above the flesh surface, (v) pausing for 2 s, (vi) lowering the stage to the next cut depth, (vii) repeating from (iii) for all depths, and (vii) repeating from (i) for all cut locations.

SUPPLEMENTARY MATERIALS

www.science.org/doi/10.1126/scirobotics.abi6745
Materials and Methods
Figs. S1 to S11
Tables S1 to S4
Movies S1 to S10
References (*60*–*63*)

REFERENCES AND NOTES

1. C. K. West, J. J. Gibson, The senses considered as perceptual systems. *J. Aesthetic Educ.* **3**, 142 (1969).
2. J. Hao, C. Bonnet, M. Amsalem, J. Ruel, P. Delmas, Transduction and encoding sensory information by skin mechanoreceptors. *Pflugers Arch. Eur. J. Physiol.* **467**, 109–119 (2015).
3. A. Rodriguez, The unstable queen: Uncertainty, mechanics, and tactile feedback. *Sci. Robot.* **6**, 4667 (2021).
4. L. Walsh, J. Critchlow, B. Beck, A. Cataldo, L. de Boer, P. Haggard, Salience-driven overestimation of total somatosensory stimulation. *Cognition* **154**, 118–129 (2016).
5. J. H. Fecteau, D. P. Munoz, Salience, relevance, and firing: A priority map for target selection. *Trends Cogn. Sci.* **10**, 382–390 (2006).
6. R. L. Klatzky, S. Lederman, C. Reed, There's more to touch than meets the eye: The salience of object attributes for haptics with and without vision. *J. Exp. Psychol. Gen.* **116**, 356–369 (1987).
7. Hsiao Steven, Gomez-Ramirez Manuel, *Neurobiology of Sensation and Reward* (CRC Press, 2011).
8. G. Colombetti, E. Thompson, in *Developmental Perspectives on Embodiment and Consciousness*, W. F. Overton, U. Müller, J. L. Newman, Eds. (Erlbaum, 2008), pp. 8–10, 12.
9. R. Koiva, T. Schwank, G. Walck, M. Meier, R. Haschke, H. Ritter, Barometer-based tactile skin for anthropomorphic robot hand, in *2020 IEEE International Conference on Intelligent Robots and Systems* (IEEE, 2020) pp. 9821–9826.
10. F. Sato, K. Takahashi, T. Abe, M. Okuyama, H. Noma, M. Sohgawa, Texture characterization including warm/cool sensation using force-, light-, and temperature-sensitive micro-electromechanical systems sensor. *Sensors and Materials.* **29**, 311–321 (2017).
11. C. Chi, X. Sun, N. Xue, T. Li, C. Liu, Recent progress in technologies for tactile sensors. *Sensors (Basel, Switzerland)* **18**, 948 (2018).
12. K. Watatani, K. Terao, F. Shimokawa, H. Takao, Planar-type MEMS tactile sensor integrating micro-macro detection function of fingertip to evaluate surface touch sensation. *Jpn. J. Appl. Phys.* **58**, 097002 (2019).
13. P. Weiner, C. Neef, T. Asfour, A multimodal embedded sensor system for scalable robotic and prosthetic fingers, in *IEEE-RAS International Conference on Humanoid Robots*. 2018 November (IEEE, 2019) pp. 286–292.
14. Y. L. Park, B. R. Chen, R. J. Wood, Design and fabrication of soft artificial skin using embedded microchannels and liquid conductors. *IEEE Sensors J.* **12**, 2711–2718 (2012).
15. J. T. Muth, D. M. Vogt, R. L. Truby, Y. Mengüç, D. B. Kolesky, R. J. Wood, J. A. Lewis, Embedded 3D printing of strain sensors within highly stretchable elastomers. *Adv. Mater.* **26**, 6307–6312 (2014).

16. C. C. Kim, H. H. Lee, K. H. Oh, J. Y. Sun, Highly stretchable, transparent ionic touch panel. *Science* **353**, 682–687 (2016).
17. J. Wissman, T. Lu, C. Majidi, Soft-matter electronics with stencil lithography, in *Proceedings of IEEE Sensors* (IEEE, 2013), pp. 1–4.
18. M. S. Sarwar, Y. Dobashi, C. Preston, J. K. M. Wyss, S. Mirabbasi, J. David, W. Madden, Bend, stretch, and touch: Locating a finger on an actively deformed transparent sensor array. *Sci. Adv.* **3**, e1602200 (2017).
19. R. Di Giacomo, L. Bonanomi, V. Costanza, B. Maresca, C. Daraio, Biomimetic temperature-sensing layer for artificial skins. *Sci. Robot.* **2**, eaai9251 (2017).
20. I. You, D. G. MacKanic, N. Matsuhisa, J. Kang, J. Kwon, L. Beker, J. Mun, W. Suh, T. Y. Kim, J. B. H. Tok, Z. Bao, U. Jeong, Artificial multimodal receptors based on ion relaxation dynamics. *Science* **370**, 961–965 (2020).
21. H. Zhao, K. O'Brien, S. Li, R. F. Shepherd, Optoelectronically innervated soft prosthetic hand via stretchable optical waveguides. *Sci. Robot.* **1**, eaai7529 (2016).
22. P. A. Xu, A. K. Mishra, H. Bai, C. A. Aubin, L. Zullo, R. F. Shepherd, Optical lace for synthetic afferent neural networks. *Sci. Robot.* **4**, eaaw6304 (2019).
23. H. Bai, S. Li, J. Barreiros, Y. Tu, C. R. Pollock, R. F. Shepherd, Stretchable distributed fiber-optic sensors. *Science* **370**, 848–852 (2020).
24. C. To, T. L. Hellebrekers, Y. L. Park, Highly stretchable optical sensors for pressure, strain, and curvature measurement, in *2015 IEEE International Conference on Intelligent Robots and Systems* (IEEE, 2015), pp. 5898–5903.
25. I. M. Van Meerbeek, C. M. De Sa, R. F. Shepherd, Soft optoelectronic sensory foams with proprioception. *Sci. Robot.* **3**, eaau2489 (2018).
26. W. Yuan, S. Dong, E. H. Adelson, GelSight: High-resolution robot tactile sensors for estimating geometry and force. *Sensors (Switzerland)* **17**, 2762 (2017).
27. M. Lambeta, P.-W. Chou, S. Tian, B. Yang, B. Maloon, V. R. Most, D. Stroud, R. Santos, A. Byagowi, G. Kammerer, D. Jayaraman, R. Calandra, DIGIT: A novel design for a low-cost compact high-resolution tactile sensor with application to in-hand manipulation. *IEEE Robotics and Automation Letters.* **5**, 3838–3845 (2020).
28. D. F. Gomes, Z. Lin, S. Luo, GelTip: A finger-shaped optical tactile sensor for robotic manipulation, in *2020 IEEE/RSJ International Conference on Intelligent Robots and Systems (IROS)* (IEEE, 2020), pp. 9903–9909.
29. C. Trueeb, C. Sferrazza, R. D'Andrea, Towards vision-based robotic skins: A data-driven, multi-camera tactile sensor, in *2020 Third IEEE International Conference on Soft Robotics (RoboSoft)* (IEEE, 2020), pp. 333–338.
30. C. Sferrazza, A. Wahlsten, C. Trueeb, R. D'Andrea, Ground truth force distribution for learning-based tactile sensing: A finite element approach. *IEEE Access*. **7**, 173438–173449 (2019).
31. A. Mkhitaryan, D. Burschka, Vision based haptic multisensor for manipulation of soft, fragile objects, in *2012 IEEE SENSORS* (IEEE, 2012), pp. 1–4.
32. H. Sun, K. J. Kuchenbecker, G. Martius, A soft thumb-sized vision-based sensor with accurate all-round force perception. arXiv:2111.05934 [cs.RO] (10 November 2021).
33. A. Agarwal, T. Man, W. Yuan, Simulation of vision-based tactile sensors using physics based rendering. arXiv:2012.13184 [cs.RO] (24 December 2020).
34. A. Alspach, K. Hashimoto, N. Kuppuswamy, R. Tedrake, Soft-bubble: A highly compliant dense geometry tactile sensor for robot manipulation. arXiv:1904.02252 [cs.RO] (3 April 2019).
35. R. S. Johansson, Å. B. Vallbo, Tactile sensory coding in the glabrous skin of the human hand. *Trends Neurosci.* **6**, 27–32 (1983).
36. Y. Jin, Y. Lin, A. Kiani, I. D. Joshipura, M. Ge, M. D. Dickey, Materials tactile logic via innervated soft thermochromic elastomers. *Nat. Commun.* **10**, 4187 (2019).
37. A. C. Siegel, S. T. Phillips, B. J. Wiley, G. M. Whitesides, Thin, lightweight, foldable thermochromic displays on paper. *Lab Chip* **9**, 2775–2781 (2009).
38. M. Friškovec, R. Kulčar, M. K. Gunde, Light fastness and high-temperature stability of thermochromic printing inks. *Color. Technol.* **129**, 214–222 (2013).
39. J. D. Willard, X. Jia, S. Xu, M. Steinbach, V. Kumar, Integrating physics-based modeling with machine learning: A survey. arXiv:2003.04919 [physics.comp-ph] (10 March 2020).
40. J. Deglint, F. Kazemzadeh, D. Cho, D. A. Clausi, A. Wong, Numerical demultiplexing of color image sensor measurements via non-linear random forest modeling. *Sci. Rep.* **6**, 28665 (2016).
41. S. Y. Won, H. K. Kim, M. E. Kim, K. S. Kim, Two-point discrimination values vary depending on test site, sex and test modality in the orofacial region: A preliminary study. *J. Appl. Oral Sci.* **25**, 427–435 (2017).
42. C. Zhang, A. Bedri, G. Reyes, B. Bercik, O. T. Inan, T. E. Starner, G. D. Abowd, TapSkin: Recognizing on-skin input for smartwatches, in *Proceedings of the 2016 ACM International Conference on Interactive Surfaces and Spaces: Nature Meets Interactive Surfaces, ISS 2016* (ACM, 2016), pp. 13–22.
43. X. D. Pang, H. Z. Tan, N. I. Durlach, Manual discrimination of force using active finger motion. *Percept. Psychophys.* **49**, 531–540 (1991).
44. T. Oroszi, M. J. G. van Heuvelen, C. Nyakas, E. A. van der Zee, Vibration detection: Its function and recent advances in medical applications. *F1000Research* **9**, F1000 (2020).
45. J. W. Ring, R. de Dear, Temperature transients: A model for heat diffusion through the skin, thermoreceptor response and thermal sensation. *Indoor Air* **1**, 448–456 (1991).
46. H. Molinari, J. D. Greenspan, D. Krenshalo, The effect of rate of temperature change and adapting temperature on thermal sensitivity. *Sens. Processes* **1**, 354–362 (1977).
47. Q. Zhang, G. Chen, K. Wu, J. Shi, L. Liang, M. Lu, Self-healable and reprocessible liquid crystalline elastomer and its highly thermal conductive composites by incorporating graphene via in-situ polymerization. *J. Appl. Polym. Sci.* **138**, 49748 (2021).
48. M. D. Bartlett, N. Kazem, M. J. Powell-Palm, X. Huang, W. Sun, J. A. Malen, C. Majidi, High thermal conductivity in soft elastomers with elongated liquid metal inclusions. *Proc. Natl. Acad. Sci.* **114**, 2143–2148 (2017).
49. T. Goto, M. Iida, H. Tan, C. Liu, K. Mayumi, R. Maeda, K. Kitahara, K. Hatakeyama, T. Ito, Y. Shimizu, H. Yokoyama, K. Kimura, K. Ito, Y. Hakuta, K. Terashima, Thermally conductive tough flexible elastomers as composite of slide-ring materials and surface modified boron nitride particles via plasma in solution. *Appl. Phys. Lett.* **112**, 101901 (2018).
50. D. Wood, K. Hensley, N. Roberts, Enhanced thermal conductance of polymer composites through embeddingaligned carbon nanofibers. *AIMS Mater. Sci.* **3**, 851–861 (2016).
51. M. Burnworth, L. Tang, J. R. Kumpfer, A. J. Duncan, F. L. Beyer, G. L. Fiore, S. J. Rowan, C. Weder, Optically healable supramolecular polymers. *Nature* **472**, 334–337 (2011).
52. J. Wu, L.-H. Cai, D. A. Weitz, Tough self-healing elastomers by molecular enforced integration of covalent and reversible networks. *Adv. Mater.* **29**, 1702616 (2017).
53. L. Zhang, D. Wang, L. Xu, X. Zhang, A. Zhang, Y. Xu, A highly stretchable, transparent, notch-insensitive self-healing elastomer for coating. *J. Mater. Chem. C* **8**, 2043–2053 (2020).
54. Y. Bengio, J. Louradour, R. Collobert, J. Weston, Curriculum learning, in *Proceedings of the 26th Annual International Conference on Machine Learning* (2009), pp. 41–48.
55. J. Tobin, R. Fong, A. Ray, J. Schneider, W. Zaremba, P. Abbeel, Domain randomization for transferring deep neural networks from simulation to the real world, in *2017 IEEE/RSJ International Conference on Intelligent Robots and Systems (IROS)* (IEEE, 2017), pp. 23–30.
56. M. Moayyedian, Intelligent optimization of mold design and process parameters in injection molding. *Springer Theses* 10.1007/978-3-030-03356-9 (2019).
57. V. Gupta, R. Jain, M. L. Meena, G. S. Dangayach, Six-sigma application in tire-manufacturing company: A case study. *J. Ind. Eng. Int.* **14**, 511–520 (2017).
58. Google Inc., Welcome to Colaboratory (2020); https://colab.research.google.com.
59. F. Pedregosa, G. Varoquaux, A. Gramfort, V. Michel, B. Thirion, O. Grisel, M. Blondel, P. Prettenhofer, R. Weiss, V. Dubourg, J. Vanderplas, A. Passos, D. Cournapeau, M. Brucher, M. Perrot, É. Duchesnay, Scikit-learn: Machine learning in python. *J. Mach. Learn. Res.* **12**, 2825–2830 (2011).
60. O. A. Shergold, N. A. Fleck, D. Radford, The uniaxial stress versus strain response of pig skin and silicone rubber at low and high strain rates. *Int. J. Impact Eng.* **32**, (2006).
61. K. Larson, Can you estimate modulus from durometer hardness for silicones? White paper, Dow Corning Corporation (2016).
62. B. Mosadegh, P. Polygerinos, C. Keplinger, S. Wennstedt, R. F. Shepherd, U. Gupta, J. Shim, K. Bertoldi, C. J. Walsh, G. M. Whitesides, Pneumatic networks for soft robotics that actuate rapidly. *Adv. Funct. Mater.* **24**, 2163–2170 (2014).
63. M. Christ, N. Braun, J. Neuffer, A. W. Kempa-Liehr, Time series FeatuRe extraction on basis of scalable hypothesis tests (tsfresh – A Python package). *Neurocomputing* **307**, 72–77 (2018).

Funding: This work was supported by the U.S. Air Force Office of Scientific Research (grant FA9550-18-1-0243) and NSF EFRI program (grant EFMA-1830924). The index of refraction data was measured at the Cornell NanoScale Facility, a member of the National Nanotechnology Coordinated Infrastructure, which is supported by the NSF (grant number ECCS-1542081). Last, this work made use of the Cornell Center for Materials Research Shared Facilities, which are supported through the NSF Materials Research Science and Engineering Centers program (DMR-1719875). **Author contributions:** J.A.B. conceived the robotic flesh, designed and conducted experiments, analyzed data, and wrote the manuscript. A.X. ran experiments and wrote the manuscript. S.P. ran experiments and analyzed thermochromics' data. G.T. edited the manuscript. N.I. and S.H. ran data collection experiments and manufacturing. A.C. coded the feature extractor module and preliminary experiments. B.S. supervised the ML research. R.F.S. supervised the research, designed and ran experiments, and edited the manuscript. **Competing interests:** R.F.S. is a cofounder of Organic Robotics Corporation that licenses some patents covered here, including publication no. 63/064,339 PCT/US20. The other authors declare that they have no competing interests. **Data and materials availability:** All data needed to evaluate the conclusions in the paper are present in the main text and the Supplementary Materials.

Submitted 24 March 2021
Accepted 15 May 2022
Published 8 June 2022
10.1126/scirobotics.abi6745

Science Robotics

Haptic perception using optoelectronic robotic flesh for embodied artificially intelligent agents

Jose A. Barreiros, Artemis Xu, Sofya Pugach, Narahari Iyengar, Graeme Troxell, Alexander Cornwell, Samantha Hong, Bart Selman, and Robert F. Shepherd

Sci. Robot. **7** (67), eabi6745. DOI: 10.1126/scirobotics.abi6745

Science Robotics (ISSN 2470-9476) is published by the American Association for the Advancement of Science. 1200 New York Avenue NW, Washington, DC 20005. The title *Science Robotics* is a registered trademark of AAAS.